Electronic Supplementary Material (ESI) for ChemComm.

Supporting information

For the manuscript

Exact distance measurements for structure and dynamics in solid proteins by fast-magic-angle-spinning NMR.

*Kristof Grohe[a,b], Evgeny Nimerovsky[c], Himanshu Singh[a,b], Suresh K. Vasa[a,b], Benedikt Söldner[a], Beat Vögeli[d], Chad M. Rienstra[c] and Rasmus Linser[a,b]**

[a] K. Grohe, Dr. H. Singh, Dr. S. K. Vasa, B. Söldner, Prof. Dr. R. Linser

Faculty for Chemistry and Pharmacy
Ludwig-Maximilians-University Munich
Butenandtstr. 5-13, 81377 Munich, Germany
*E-mail: rasmus.linser@lmu.de

[b] K. Grohe, Dr. H. Singh, Dr. S. K. Vasa, Prof. Dr. R. Linser

Faculty for Chemistry and Chemical Biology,
Technical University Dortmund,
Otto-Hahn-Straße 4a, 44227 Dortmund, Germany

[c] Dr. E. Nimerovsky, Prof. Dr. C. M. Rienstra

Department of Chemistry
University of Illinois
600 South Mathews Avenue
Urbana, IL 61801, United States of America

[d] Prof. Dr. B. R. Vögeli

Department of Biochemistry and Molecular Genetics,
University of Colorado Denver,
12801 East 17th Avenue,
Aurora, CO 80045, United States of America.

Experimental section

The perdeuterated, ^{13}C- and ^{15}N-labeled samples of chicken α-spectrin SH3 domain and human carbonic anhydrase II (hCAII) were expressed and purified as described earlier[1,2], with exchangeable sites back-exchanged along purification in 100 % H_2O. For NMR experiments approximately 1 mg of Cu-EDTA-doped protein[3] was needed each. NMR experiments were carried out at 700 MHz proton Larmor frequency and 55.55 kHz MAS frequency, using a standard-bore 1.3 mm triple-resonance probe on a Bruker AVANCE NEO spectrometer at approximately 20 °C. RFDR spectra were recorded for 0.29, 0.43, 0.58, 0.72, 0.86, 1.01, 1,15, 1.44, 1.73, 2.02, 2.30, 2.88, 3.46, and 4.03 ms RFDR mixing time for SH3 and 0.18, 0.31, 0.61, 0.86, 1.15, 1.44, 2.02, 2.88, 4.03, 4.90, and 5.76 ms mixing time for hCAII. The 180° pulse during RFDR had a pulse length of 3 µs, resulting in a duty factor of 0.16 and an *rf* frequency of 166.6 kHz. 25 ms t_{1max} in the ^{15}N, 20 ms in the indirect ^{1}H, and 50 ms acquisition time in the direct ^{1}H-dimension were used. The experimental time of each 3D spectrum was approximately 20.5 hours. (The first 4 mixing times (up to 1 ms) were sufficient for the analysis (see Fig S4), which leads to a total experimental time of 82 hours or 3.5 days.) Data processing and assignments were carried out using Topspin 4 and CcpNMR[4], respectively with determination of peak intensities as peak heights.

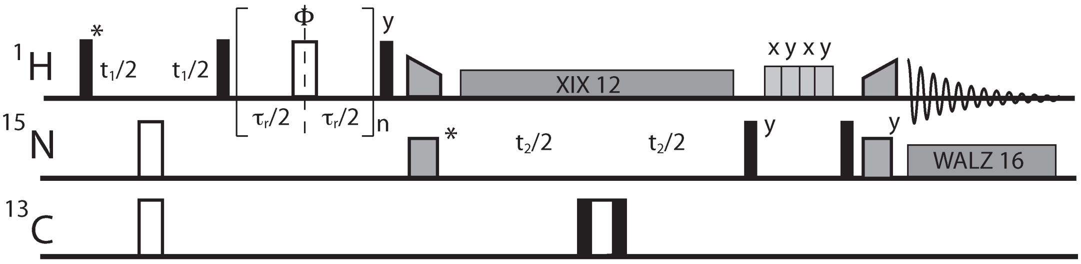

Fig. S1: Pulse scheme for the 3D ^{15}N-edited ^{1}H-^{1}H RFDR experiment.[5,6] Filled and open bars represent 90 and 180 ° pulses, respectively. Water suppression (light gray shapes) was achieved using similar means as proposed by Zhou et al.[7] Asterisks denote phase-sensitive incrementation according to States-TPPI, the phase ϕ represents an XY-8[8] phase cycle during the RFDR mixing. CP (non-annotated dark gray shapes) duration amounted to 300 µs and used an 80-100% ramp on the proton channel. Decoupling during indirect and direct acquisition was performed using XiX-12[9] at 14 kHz and WALTZ-16[10] at 10 kHz, respectively. t_{1max} and t_{2max} amounted to 20 and 25 ms, respectively. The counter *n* was chosen such that overall RFDR mixing times were achieved as denoted in the main text.

Numerical powder-averaged two-spin-model simulations of ^{1}H-RFDR cross-peak buildups were obtained using an in-house MATLAB[11] script, setting inter-proton distances from 2.0 to 8 Å, and normalizing the intensity to the diagonal-peak, which was simulated equally.

Structure calculations were performed using CNS1.1[12] calculating 300 trial structures with 15000 steps in the first and 220000 steps in the second slow-cooling annealing stage. The eRFDR structure calculation depicted in Figure 4C (main text) was carried out using the available 45 unidirectional and 30 bidirectional eRFDR restraints (as shown on the average structure in Figure 4B, main text), in addition to 47 conventional RFDR restraints as well as dihedral-angle restraints. In terms of comparison, a structure calculation using 122 conventional RFDR restraints in addition to dihedral-angle restraints, as shown in Figure 4A, was performed. In order to create an objective measure for the quality of structural improvement using eRFDR restraints, we grouped all unambiguous cross-peaks from the 2 ms mixing time dataset by their intensity relative to the diagonal peak, creating three tiers: Peaks showing an intense relative cross peak were considered close and converted into a restraint with an upper distance limit of 5 Å. Peaks showing a medium or a small relative cross peak intensity were considered intermediate or far, with an upper distance limit of 7.5 Å and 9 Å, respectively. The computational time for structure calculation amounted to approximately 1.5 days on one core (an Intel i7 processor).

Data processing to generate eRFDR-restraints by help of eNORA2

In order to generate exact distance restraints from RFDR buildup the following error sources have to be addressed: *i*) Site specificity of the polarization transfer efficiency during the heteronuclear correlation part. *ii*) Site-specific relaxation and pulse imperfections. *iii*) Relayed polarization transfer via third spins.

In order to correct for differential polarization transfer efficiency, the cross-peak buildup $H_j \rightarrow H_i$ is divided by the diagonal-peak intensity at zero mixing time $I_{ii}(0)$,

$$I_{ji,norm}(t) = \frac{I_{ji}(t)}{I_{ii}(0)} \quad , \tag{S1}$$

which is extrapolated from a mono-exponential fit.

$$I_{ii}(t) = I_{ii}(0) \cdot e^{-k_{ii}t} \,. \tag{S2}$$

$I_{ii}(t)$ is the diagonal-peak intensity of spin i measured at mixing time t, $I_{ii}(0)$ is the diagonal-peak intensity of spin i at zero mixing time, and k_{ii} represents the decay rate of the diagonal peak. While in liquid-state NOESY k_{ii} is the auto-relaxation rate of spin i, this behavior is dominated by losses induced by the RFDR pulse train in the solid-state counterpart. In the normalized intensity the polarization transferred via neighboring spins in terms of spin diffusion is corrected using an initial structural model, considering all relay pathways in addition to the direct transfer:

$$I_{ji,corr}(t) = p_{ji}(t) \cdot I_{ji,norm}(t) \,, \tag{S3}$$

$I_{norm}(t)$ being the cross-peak intensity normalized with the diagonal-peak intensity at zero mixing time, $I_{corr}(t)$ the corrected cross-peak intensity, and $p(t)$ the correction coefficient for intensities at mixing time t. (For more details see Orts et al.[13])

The correction coefficient *p(t)* can be derived on the basis of the spin network geometries using either the simulated cross-peak intensity originating from polarization relay-transferred through individual third spins (option “three spin” in the masterscript of eNORA2):[13]

$$p(t) = \frac{I_{twospin}(t)}{I_{twospin}(t)+\sum_n\left(I_{threespin}{}^{n}(t)-I_{twospin}(t)\right)} \tag{S4.1}$$

Alternatively, *p(t)* can be derived from the simulated ratio of the transfers in a two-spin system and in a multi-spin system, if the option “full matrix” is chosen:[14]

$$p(t) = \frac{I_{twospin}(t)}{I_{multispin}(t)} \tag{S4.2}$$

$I_{twospin}(t)$ is the simulated intensity using an ideal two-spin model and $I_{threespin}$ or $I_{multispin}^{(n)}(t)$ (using the option “three spin” or “full matrix”, respectively) the simulated intensity originating from polarization transfer through the neighboring spins within spheres of a user-chosen radius (12 Å in this study). Whereas the data shown in the manuscript is based on the “three-spin approach”, no significant differences were observed upon usage of the “full-matrix approach”

In order to further correct for polarization loss during application of the RFDR pulse train, the diagonal-peak decay k_{ii} values obtained from fits in equation S2 are used as fixed input values to extract the cross-relaxation rates from fits of the buildup intensities $I_{ij}(t)$ and $I_{ji}(t)$.

For description of any magnetization transfers, eNORA uses the solution for the Solomon equation, which for a two-spin system is:

$$\frac{I_{ij}(t)}{I_{ii}(0)} = \frac{I_{ji}(t)}{I_{jj}(0)} = \frac{-\sigma_{ij}}{\lambda_+ - \lambda_-}\left[e^{-\lambda_- t} - e^{-\lambda_+ t}\right] \tag{S5}$$

with

$$\lambda_\pm = \frac{\left(k_{ii}+k_{jj}\right)}{2} \pm \sqrt{\left(\frac{k_{ii}-k_{jj}}{2}\right)^2 + \sigma_{ij}^2} \quad , \tag{S6}$$

where σ_{ij} is the magnetization transfer rate between protons H_i and H_j, and k_{ii} was the diagonal decay rate of the proton H_i.

For simulation of relay transfers, eNORA2 makes use of the transfer matrix describing the time evolution of all possible cross peak intensities.

$$I(t) = I(0) \cdot e^{-Rt} \tag{S7}$$

With

$$R = \begin{pmatrix} k_{11} & \sigma_{12} & \dots \sigma_{1N} \\ \sigma_{21} & k_{22} & \dots \sigma_{2N} \\ \sigma_{N1} & \sigma_{N2} & \dots k_{NN} \end{pmatrix} \tag{S8}$$

"Bidirectional" distance restraints were obtained using the average of the build-up rate σ of cross-peaks $H_j \rightarrow H_i$ and $H_i \rightarrow H_j$:

$$\sigma_{bidir} = sqrt(\sigma_{ij}\sigma_{ji}) \tag{S9}$$

The first-order dipolar recoupling Hamiltonian during RFDR being dependent on r^{-3} terms, the buildups were associated with distances using the equation

$$y = a \cdot r^{-3}. \tag{S10}$$

The computational time for the relay transfer correction is approximately 2 minutes using one core of an Intel i7 processor.

Comparison of distance correlation functions

In solution state NMR, the mechanism for through-space polarization transfer is precisely known as cross relaxation according to zero- and double-quantum transitions and described by the Solomon equation.[15]

$$\sigma_{ij} = \left(\frac{\mu_0}{4\pi}\right)^2 \cdot \frac{\gamma^4 h^2}{10} \tau_c \cdot r^{-6} \tag{S11}$$

By contrast, in the case of RFDR, the practical consequences of polarization transfer with respect to the relation between effective transfer rate and internuclear distance is not fully understood. The effective Hamiltonian of (finite-pulse) RFDR scales inversely with the MAS rotor frequency and is dependent on various other parameters. Artifacts resulting from varying chemical shift differences between recoupled nuclei are removed by super-cycles (in this case XY-8), which eliminate higher-order (cross) terms in the average Hamiltonian. From a theoretical analysis using a quantized-field approach/average Hamiltonian theory, or Floquet theory, transfer probability of RFDR in a two-spin system is expected to scale with r^{-3}, as a coherent-driven type of transfer.[16] However, for multi-spin interactions in praxis a less clear dependency, effectively somewhere between r^{-3} and r^{-6}, has been described.[17] As the correlation known from proton-driven spin diffusion[18] has been experimentally found to be proportional to r^{-6}, we were interested to experimentally determine the practically most relevant expression, assuming any potency between r^{-3} and r^{-6} (Figure S2 and S3)

$$\sigma_{ij} = a \cdot r^{-x} + b \tag{S12}$$

Figure S3 shows uni- and bidirectional eRFDR restraints analyzed using an adapted version of the freely available program eNORA2[19]. In order to determine the most useful correlation between buildup rate and distance we modified the program by changing the functions for distance determination and relay transfer correction according to equation S12 with $x = 3$, 4, 5, and 6. Interestingly, the R^2 values of the four different correlations of measured versus X-ray distances of SH3 show very similar values of around 0.9. Regarding this consistency, for further analysis we still used the correlation function containing r^{-3}, since this represents the first-order average Hamiltonian for dipolar recoupling.

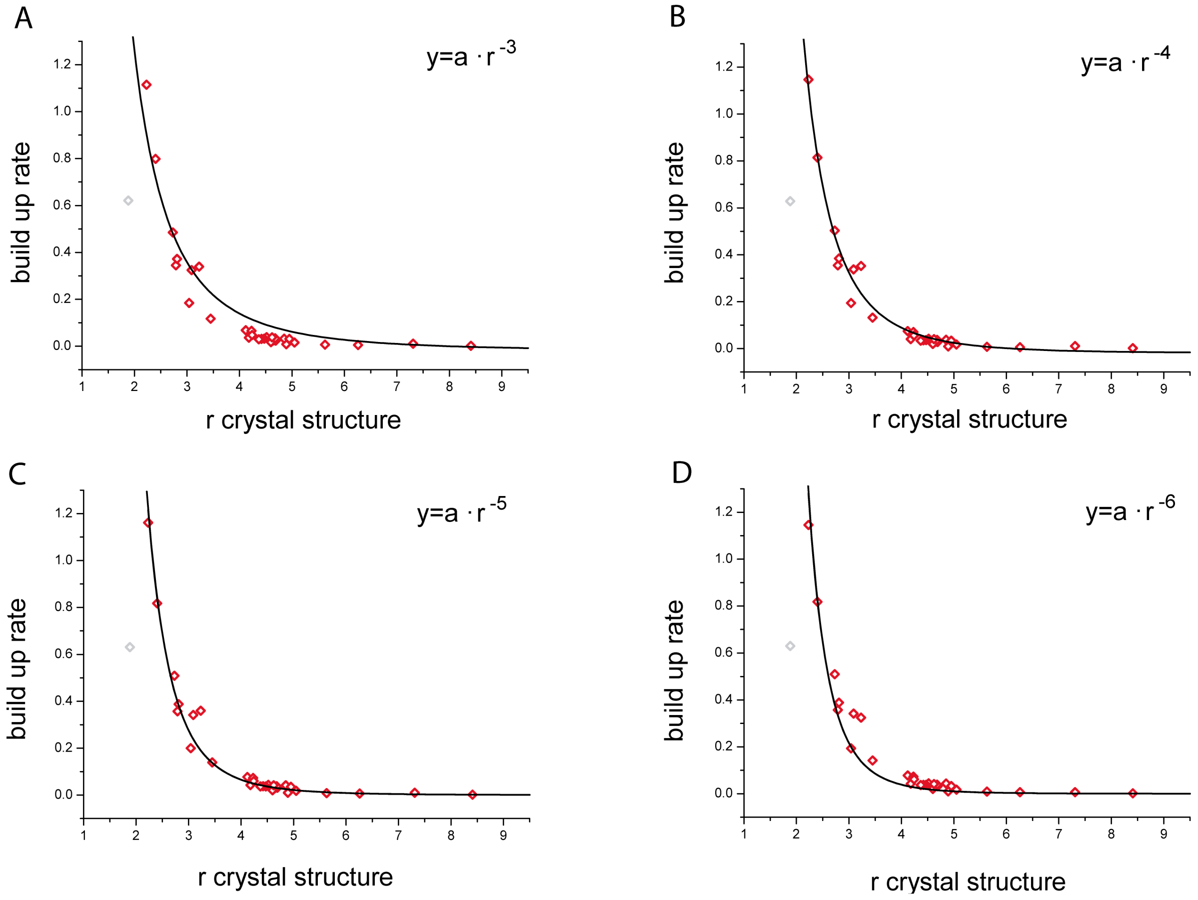

Figure S2. Buildup rates obtained by eNORA2 as a function of the distance read out from the crystal structure 2NUZ. **A-D:** The plotted buildup curves were corrected for spin diffusion using the full-transfer-matrix approach considering an r^{-3}, r^{-4}, r^{-5}, or r^{-6} buildup-distance correlation and fitted with the equation shown in the respective figure. The data point with shortest amide-amide distance (shown in gray) stands out from the expected behavior. For this pair with unusually short distance (residues 18 and 19), the protons are at the tip of a dynamic loop.[20] As such, at room temperature, both their effective distance is expected to be increased and their dipolar interaction is reduced. Compare Figures S3 and S10A. (This pair is omitted from the fit, also see below.)

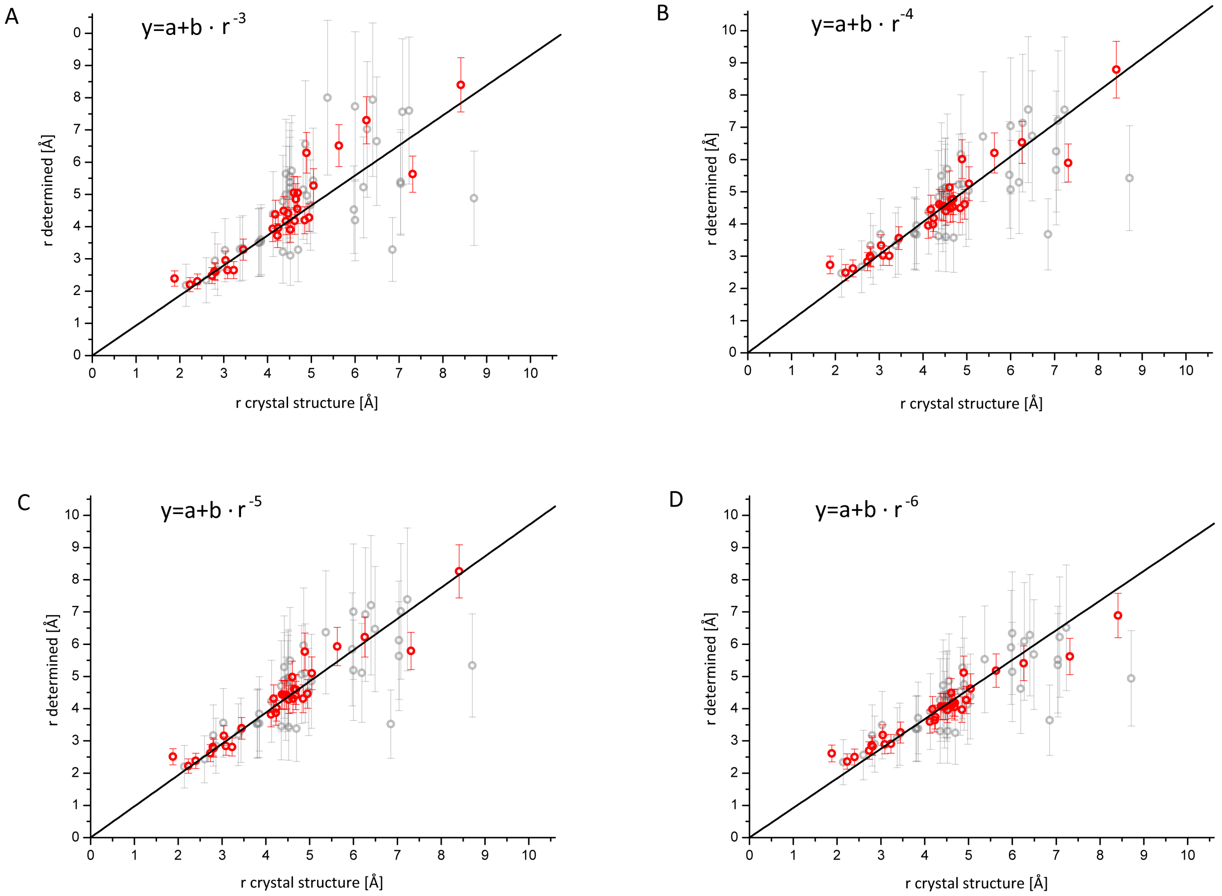

Figure S3. Correlations between distances measured by eRFDR and distances read out from the crystal structure (2NUZ). In **A**, **B**, **C**, and **D** the eRFDR distances were determined with the equation shown in the respective figure. In all cases the measured distances correlate well with the ones read out from the crystal structure. Distances which are greater than 5.5 Å in the crystal structure show a larger deviation probably caused by dipolar truncation and increasing spin diffusion contributions. The comparison shows that the exponent of the distance dependency of the RFDR buildup is less relevant than expected. Other errors have a higher impact on the accuracy. For the data point with shortest amide-amide distance, which stands out from the expected behavior, this is most probably due to loop dynamics (see above, also compare Figures S2 and S10).

Validation of uniform fitting up to 1 ms of mixing time

In order to practically apply the initial-regime approach to the experimental data, the transfers were grouped into "fast buildup", in which intensities were fitted till 1 ms mixing time, and "slow-buildup", which were fitted till 2 ms mixing time, based on the time point when the maximum intensity is reached. For purely automated data processing we also verified if buildups could be fitted absolutely uniformly (without manual interference), therefore we fitted all cross peaks only till 1 ms mixing time. In fact, this only shows minor differences regarding the determined distances (see Figures S4 and S8) and at the same time demonstrates that RFDR buildups consisting of 4 to 5 spectra (here with a total experimental time of around 80 hours) are fully sufficient to determine eRFDR restraints.

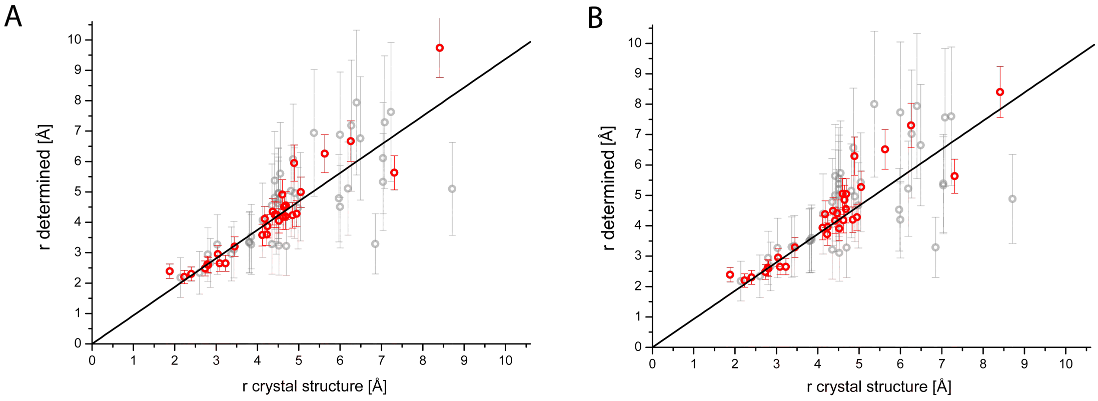

Figure S4. Validation of uniformly fitting up to 1 ms of mixing time. **A)** Bidirectional (red) and unidirectional (gray) eRFDR restraints, determined by fitting the cross peaks of fast buildup with a fit up to 1ms and those with slower buildup with a fit up to 2 ms of mixing time. **B)** eRFDR restraints determined by fitting all peaks uniformly up to 1 ms of mixing time.

Verification of the applied analytical routines using powder-averaged numerical simulations

In the course of verifying the used data processing approach, we run powder-averaged 2- and 3-spin simulations and used the simulated buildup and diagonal-decay curves as an input for the modified eNORA2 program. We used an in-house written MATLAB script including the following propagators:

$$U_1 = exp\left\{-i\int_0^{0.5T_R-0.5t_p} dt\,[1.5\omega_D(t)I_{z1}I_{z2}]\right\} \tag{S13a}$$

$$U_2 = \hat{T}exp\left\{-i\int_{0.5T_R-0.5t_p}^{0.5T_R+0.5t_p} dt\,\left[1.5\omega_D(t)I_{z1}I_{z2} + \omega_{rf}(I_{x1}+I_{x2})\right]\right\} \tag{S13b}$$

$$U_3 = exp\left\{-i\int_{0.5T_R+0.5t_p}^{T_R} dt\,[1.5\omega_D(t)I_{z1}I_{z2}]\right\} \tag{S13c}$$

$$U_4 = \hat{T}exp\left\{-i\int_{0.5T_R-0.5t_p}^{0.5T_R+0.5t_p} dt\,\left[1.5\omega_D(t)I_{z1}I_{z2} + \omega_{rf}\left(I_{y1}+I_{y2}\right)\right]\right\} \tag{S13d}$$

$$U_{RFDR} = U_3 \cdot U_4 \cdot U_1 \cdot U_3 \cdot U_2 \cdot U_1 \tag{S13e}$$

where $\omega_D(t)$ is the dipolar function[21,22], dependent on time, spinning speed, and Euler angles[7], T_R is the rotor period, t_p is the width of the π – pulses, and $\hat{T}$ is the time-ordered Dyson operator.

U_2 and U_4 are corresponding to the x- and y-π pulses of an XY-8 phase cycle, respectively. A Dyson-dependent propagator can be departed in a series of N Dyson-independent propagators[23] as follows:

$$U = \hat{T}exp\left\{-i\int_0^{\tau} dtH(t)\right\} \approx e^{-i\int_{(N-1)\tau/N}^{\tau} dtH(t)} \ldots e^{-i\int_{\tau/N}^{2\tau/N} dtH(t)} e^{-i\int_0^{\tau/N} dtH(t)} \qquad \text{(S14)}$$

Figure S5 shows exemplary comparisons of the simulated buildup curve with the experimental data from the SH3 domain. The shape of the simulated curves is in good agreement with the experimental values, however, with this direct fitting (without any correction) the fitted distance is significantly off in each case.

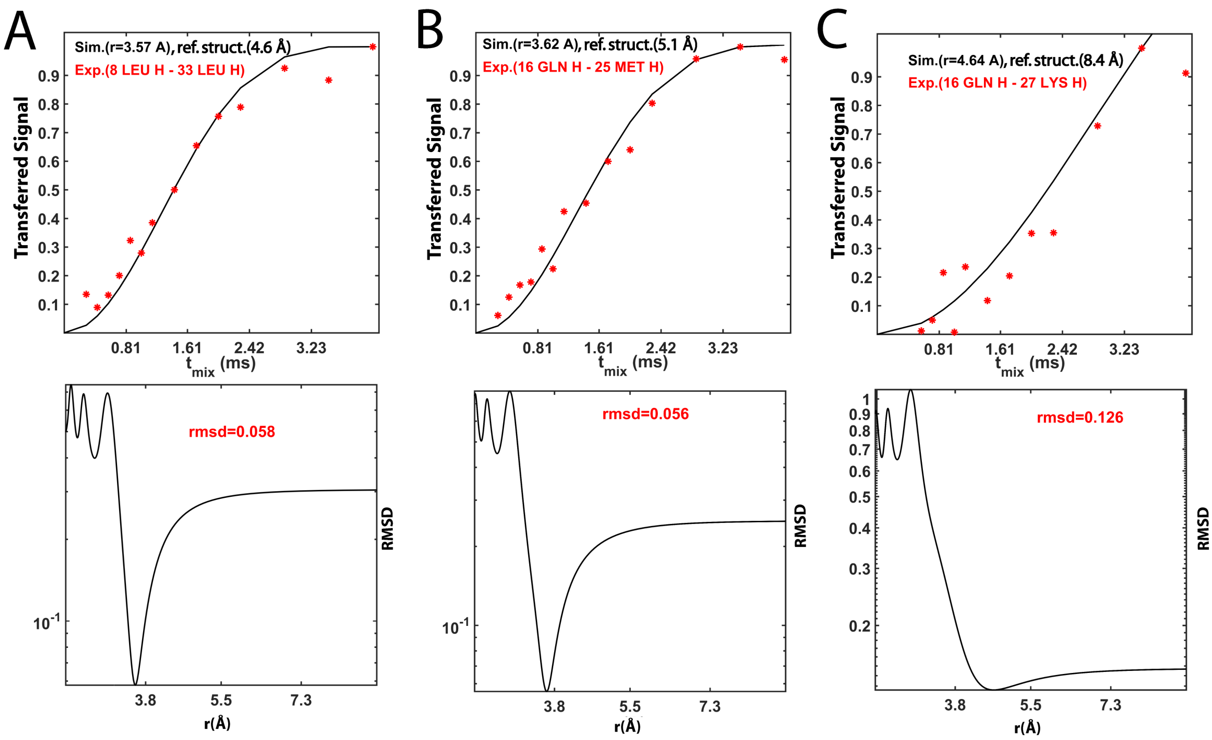

Figure S5. Comparison of experimental data (red stars) with the exact numerical 2-spin model solution (black line), directly fitting the data without correction. RFDR buildups for the exemplary distances: **A)** Leucines 8 and 33, with a distance for the best-correlating simulation of 3.6 Å and a distance read out from the crystal structure of 4.6 Å. **B)** Gln 16 and Met 25, with a distance for the best-correlating simulation of 3.6 Å and a distance read out from the crystal structure of 5.1 Å. **C)** Gln 16 and Lys 27, with a distance for the best-correlating simulation of 4.6 Å and a distance read out from the crystal structure of 8.4 Å. Bottom panels depict RMSDs between experimental data and simulated curve as a function of simulation distance.

The best-correlating simulation distances are significantly shorter than the distances read out from the crystal structure 2NUZ. This deviation, which cannot be accounted for by simple scaling using a constant factor, underlines that an uncorrected 2-spin simulation is not suitable for exact distance determination. In order to confirm the influence of spin diffusion via third spins, we performed 3-spin simulations. Figure S6 shows the simulation of Leu 8 – Leu 33, the same pair of nuclei also used in Figure S5A. In fact, the deviation of the simulated distance from the crystal structure distance is reduced, demonstrating the significance of spin diffusion via third spins. Simulations involving all spins playing a role in the polarization transfers, also involving refinement cycles that are potentially necessary, are not suitable due to computational effort. This makes the simplified analytical solution presented in this work more favorable.

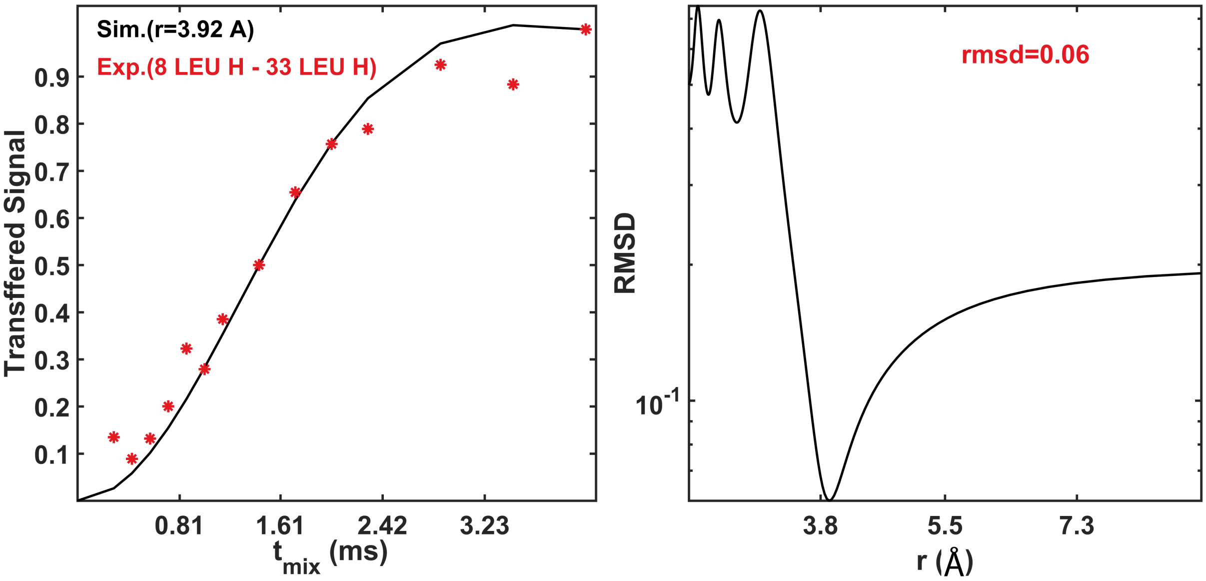

Figure S6. Powder averaged 3-spin simulation (black line) and experimental intensities (red stars) of the buildup Leu 8 – Leu 33. The distance of the third spin (to either of the two others) was set to 4.6 Å. The minimum RMSD regarding simulated curve and experimental data changed from 3.6 Å in case of the 2-spin simulation to 3.9 Å, which is closer to the crystal structure distance of 4.6 Å.

For verification of the presented analytical approach with a simplified buildup function, we conducted 2-spin model simulations as described above with inter-nuclear distances from 2 to 8 Å, spinning speed of 55.555 kHz, and a Larmor frequency of 700 MHz. The resulting buildup curves (partly shown in Figure 2B main text) were fitted up to the first maximum using a linear (Figure S7A), a trigonometric (Figure S7B), and an exponential function (Figure S7C). The resulting rates were fitted using equation S15. All fits correlate nearly perfectly with an R^2 value of above 0.99, meaning that all 3 fitting procedures would be practically suitable to determine polarization buildup rates in the initial regime. Such fitting of the initial regime only has been used in other contexts previously.[24]

$$\sigma_{ij} = a \cdot r^{-3} \tag{S15}$$

To examine further the applicability of the combined exponential fitting routines used in eNORA2, simulated cross-peak buildup and diagonal-decay intensity values were used as an input for the eNORA2 program, modified as described above. The distances determined using eNORA2 and the distances set for creating the simulated input show a good correlation (Figure S7D). According to the results of the simulations, fitting the experimental intensities exponentially represents a sufficient approximation.

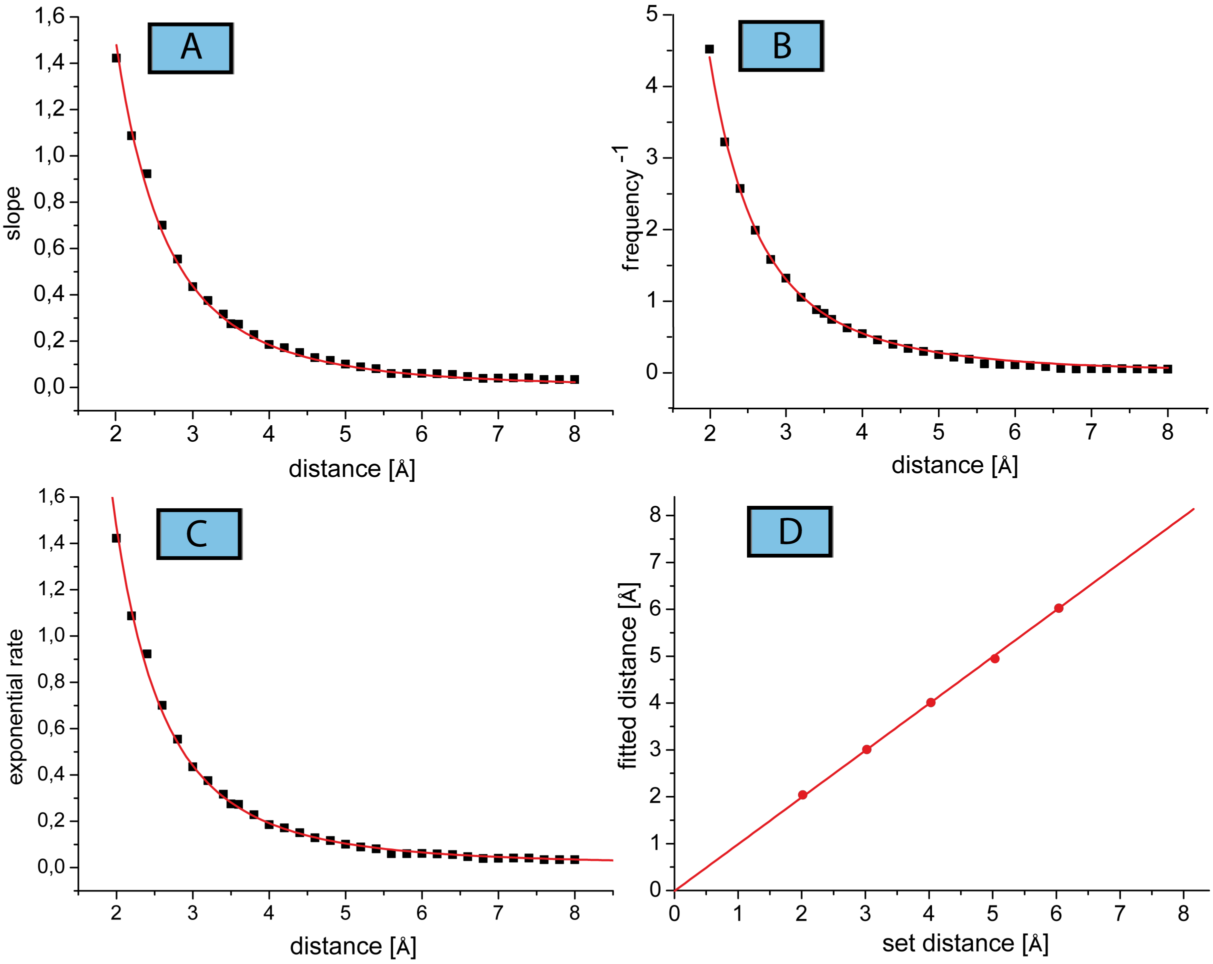

Figure S7. Comparison of different fitting routines to determine the polarization buildup rates. **A)** Linearly fitted buildup rates. **B)** Buildup rates as the inverse frequencies of a trigonometric function. **C)** Exponentially fitted buildup rates. In **A-C** simulations (compare main text Figure 2B) according to inter-nuclear distances from 2 Å up to 8 Å were fitted till the first maximum and correlated using equation S15 with a resulting R^2 value above 0.99 in all cases. **D)** Verification of the modified (exponential) fitting procedure of eNORA2 using simulated buildup and decay curves. Distances from 2 to 6 Å were used as the “experimental” input for the program eNORA2 to verify the fitting procedure. Determined distances and distances set for the simulation correlate linearly.

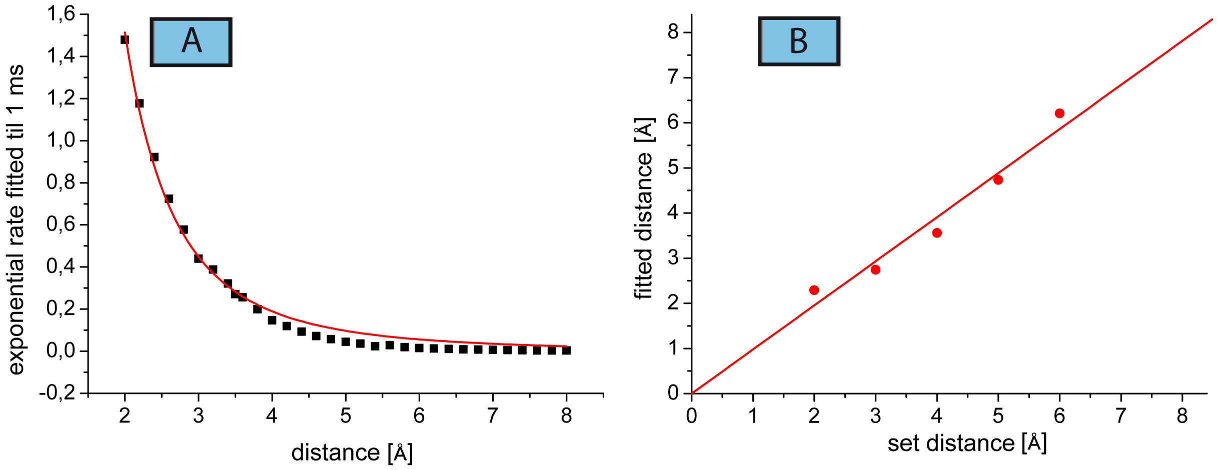

Figure S8. Fitting of the simulated buildups uniform up to 1 ms of mixing time only. **A)** Exponential buildup rates according to Figure S7C, fitted uniformly up to 1 ms of mixing time. **B**) Verification of the fitting procedure in eNORA2. Simulated buildup and decay curves up to 1 ms of mixing time, for distances from 2 to 6 Å, were used as "experimental" input for the program eNORA2, according to Figure S7D.

Modifications of eNORA for solid-state NMR RFDR

With the data processing strategies for solid-state NMR demonstrated to be applicable in the described way, it is possible to make use of the eNORA2[19] program, which was originally written for liquid-state eNOE, if modified for solid-state NMR as described in the following. The program allows to generate eRFDR restraints in a fast and convenient manner. Differences between the exact-NOE approach and the exact-RFDR approach concern the buildup behavior and the correlation of polarization transfer with internuclear distance. For the buildup behavior no simple analytical function (approximated rather via more complicated Bessel-functions sometimes) is known. However, we showed that this obstacle can be circumvented by assessing the relative magnetization transfer rate using a mono-exponential buildup function followed by a calibration. This holds perfectly true only as long as all buildups are fitted up to a comparable (relative) time point, like the first maximum of the buildup. If all buildups are fitted equally up to a fixed time, for example 1 ms, discrepancies between the fitting function and the nature of the buildup do invoke errors. However, as shown in Fig. S8, for buildups corresponding to internuclear distances in the range of 2-6 Å, in practice these errors are reasonably low. Regarding the scaling between buildup and distance, the dipolar recoupling in RFDR follows a cubic correlation when exclusively taking the first-order Hamiltonian into account. By including higher-order terms, the correlation gets less clean. Additionally, using finite-pulse RFDR, also mechanisms contribute to the polarization transfer that are different from dipolar recoupling. Consequently, our experimental data seems to obey a correlation between r^{-4} and r^{-5}. However, these differences have only a small impact on the accuracy of the determined distances, such that a cubic correlation as predicted by the first-order Hamiltonian was chosen as a good approximation.

The code of eNORA2 was modified regarding the equations for the spin diffusion correction and conversion of buildup rates into distances, which can be found in the following eNORA2 MATLAB scripts:

eNORA2/eNOEprogram/shared/R.m,

eNORA2/eNOEprogram/shared/S.m,

eNORA2/eNOEprogram/shared/sigma2distance.m.

Since the initial parameters for converging the fit are set for NOE-buildup, which covers hundreds of ms, the values of the applied RFDR mixing times should be multiplied by 1000. This factor is equated by the calibration using the input parameter correlation time τ_c in the master script.

Note:

As the distance dependency scaling exponent does not largely influence the accuracy of the distances obtained (as shown in Figures S2 and S3), it is also possible to successfully use a completely unmodified version of eNORA2 (assuming an r^{-6} dependency), which is kindly provided at the homepage of Prof. Dr. Beat Vögeli.

eRFDR distance restraints recorded for the 29kDa human carbonic anhydrase II

The triply labeled, 100% back-exchanged sample of human carbonic anhydrase II (hCAII) was prepared as described earlier[25]. NMR experiments were carried out as described in the Experimental Section. From the RFDR-spectra 176 through-space connections were assigned unambiguously. 43 of these through-space connections contain one unambiguous pair of cross- and diagonal peak, leading to unidirectional eRFDR restraints (in Figure S9A**:** orange connections, in B**:** orange cycles), and 33 contain 2 pairs of unambiguous cross- and diagonal peaks, yielding bidirectional eRFDR restraints (in Figure S9A: red connections, in B: red cycles). The determined distances and the distance read out from the crystal structure (2CBA) are in very good agreement, with an RMSD of 0.29 Å regarding bidirectional restraints shorter than 5.5 Å.

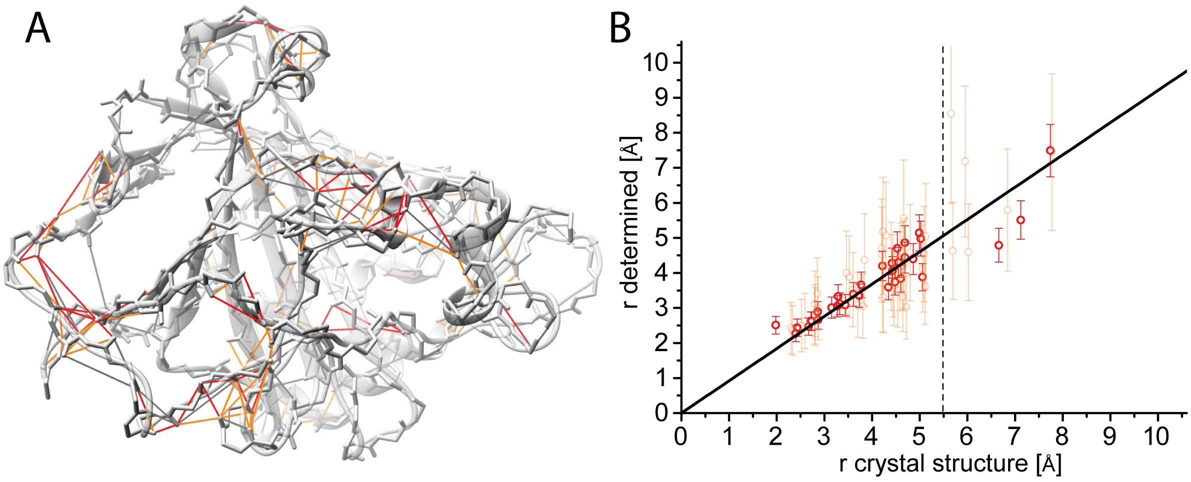

Figure S9. **A)** Bidirectional (red) and unidirectional (orange) eRFDR as well as conventional (gray) RFDR restraints depicted on the X-ray structure of carbonic anhydrase II. **B)** Correlation between bidirectional eRFDR restraints (shown in red) or unidirectional eRFDR restraints (shown in light orange) and the corresponding distances read out from the X-ray structure. The buildup curves were fitted uniformly up to 1 ms of mixing time. Distances larger than 5.5 Å show larger deviation due to error caused by dipolar truncation and strong spin diffusion. The shortest distance corresponding to HN37->HN38 shows a larger deviation presumably caused by dynamics (compare Figure S10B).

Comment to amide proton distances of residue 18 to 19 (SH3) and 37 to 38 (hCAII) according to the X-ray structures 2NUZ and 2CBA

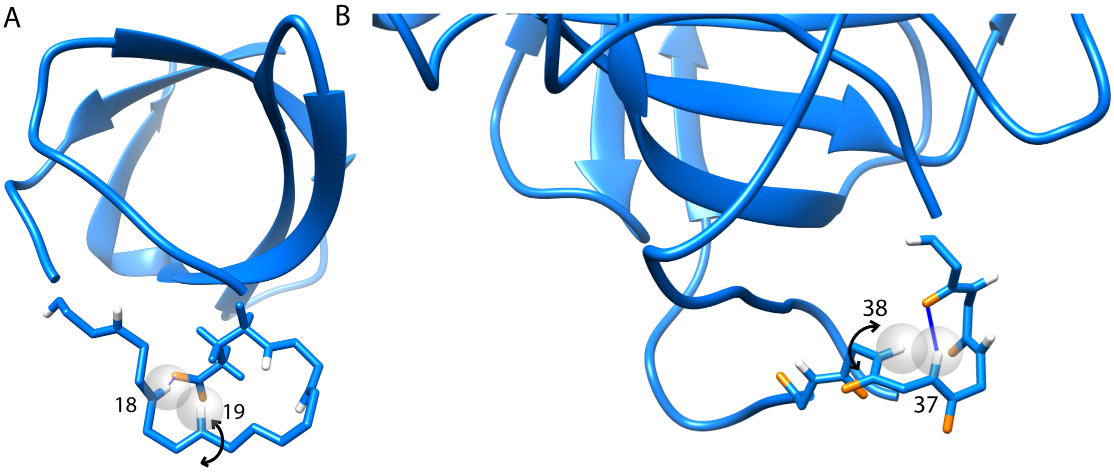

Figure S10. Depiction of the amide protons of **A)** residue 18 and 19 in the SH3 X-ray structure 2NUZ and **B)** 37 and 38 in the hCAII X-ray structure 2CBA (The distances are as small as the sum of the two van-der-Waals radii, represented by spheres). Apart from uncertainties in the reconstruction of proton locations from (heteronuclear-only) electron densities generally, both the distal loop in **A** as well as the respective loop in **B** are also known to undergo motions on different timescales[2,20,26,27]. Both effects will be sensed within the RFDR experiment, rendering the effective distance larger than what is suggested by the reference distance determined from 2NUZ and 2CBA crystal structures.

Iterative structural improvement using the eRFDR approach

Figure S11 shows that in case of deuterated and 100% backexchanged SH3, a standard solid-state NMR structure is already sufficient to successfully perform the corrections for relayed magnetization transfer via third spins. An improved structure using the eRFDR approach can be obtained in the second step. The structural precision and accuracy are equal to those of the eRFDR structure obtained when using the crystal structure in terms of correction for relayed transfer via third spins.

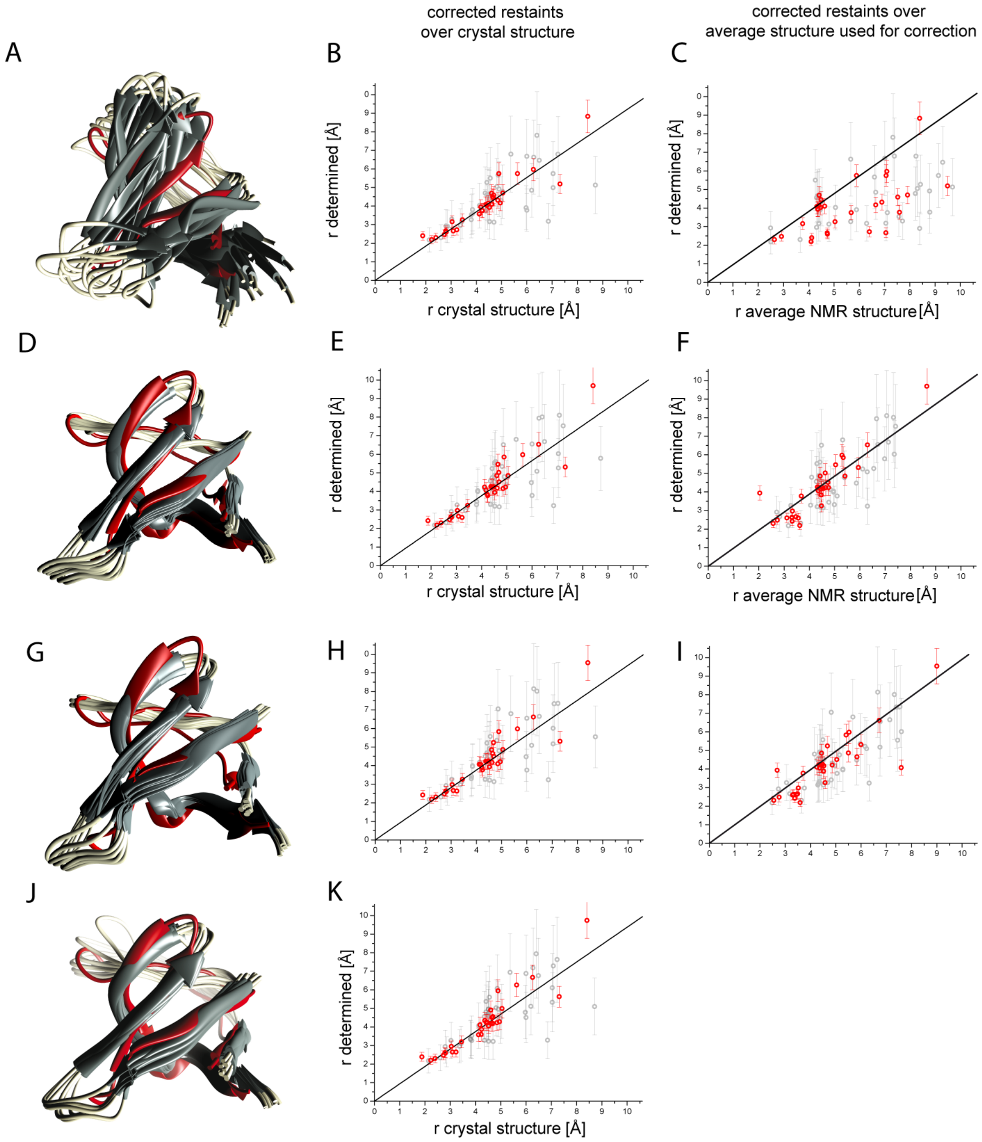

Figure S11: Structure determination using the eRFDR approach starting from standard RFDR restraints. **A)** Structural ensemble of the 10 lowest energy structures determined by conventional RFDR upper limit restraints depicted in gray, aligned with the crystal structure 2NUZ shown in red. **B)** Distance restraints obtained by using the eRFDR approach with the average structure of A employed for spin diffusion correction (in this terms spin diffusion means relayed magnetization transfer via third spins) plotted over the corresponding internuclear distances of the crystal structure 2NUZ. **C)** Distance restraints obtained by using the eRFDR approach plotted over the internuclear distances of the average structure of the ensemble in A. **D)** Structural ensemble of the 10 lowest energy structures determined by the eRFDR-restraints obtained by using the average structure of A for spin diffusion correction. **E)** Distance restraints obtained by using the average structure of D for relay transfer correction plotted over the corresponding internuclear distances of the crystal structure 2NUZ. **F)** Distance restraints obtained by using the eRFDR approach plotted over the internuclear distances of the average structure of the ensemble in D. **G-I)** Additional refinement iteration just as described for E-F. **J)** Structural ensemble of the 10 lowest-energy structures obtained by using the eRFDR approach employing the crystal structure 2NUZ for relay transfer correction. **K)** Distance restraints obtained by using the eRFDR approach with the crystal structure employed for relay transfer correction.

Supplementary literature:

1. R. Linser, V. Chevelkov, A. Diehl and B. Reif, *J. Magn. Reson.*, 2007, **189**, 209-216.
2. S. K. Vasa, H. Singh, P. Rovó and R. Linser, *J. Phys. Chem. Lett.*, 2018, **9**, 1307−1311.
3. R. Linser, V. Chevelkov, A. Diehl and B. Reif, *J. Magn. Reson.*, 2007, **189**, 209–216.
4. W. F. Vranken, W. Boucher, T. J. Stevens, R. H. Fogh, A. Pajon, M. Llinas, E. L. Ulrich, J. L. Markley, J. Ionides and E. D. Laue, *Proteins: Structure, Function, and Bioinformatics*, 2005, **59**, 687-696.
5. D. H. Zhou, J. J. Shea, A. J. Nieuwkoop, W. T. Franks, B. J. Wylie, C. Mullen, D. Sandoz and C. M. Rienstra, *Angew. Chem., Int. Ed.*, 2007, **46**, 8380-8383.
6. R. Linser, B. Bardiaux, V. Higman, U. Fink and B. Reif, *J. Am. Chem. Soc.*, 2011, **133**, 5905-5912.
7. Z. Zhou, R. Kümmerle, X. Qiu, D. Redwine, R. Cong, A. Taha, D. Baugh and B. Winniford, *J. Magn. Reson.*, 2007, **187**, 225-233.
8. T. Gullion, D. B. Baker and M. S. Conradi, *J. Magn. Reson.* , 1990, **89**, 479.
9. M. Ernst, A. Samoson and B. H. Meier, *J. Magn. Reson.*, 2003, **163**, 332-339.
10. A. J. Shaka, J. Keeler, T. Frenkiel and R. Freeman, *J. Magn. Reson.*, 1983, **52**, 335-338.
11. Matlab, *The MathWorks, Inc.*, R2011b.
12. P. D. A. A.T. Brünger, G.M. Clore, P.Gros, R.W. Grosse-Kunstleve, J.-S. Jiang, J. Kuszewski, N. Nilges, N.S. Pannu, R.J. Read, L.M. Rice, T. Simonson, G.L. Warren, *Acta Cryst.D54*, 1998, 905-921.
13. J. Orts, B. Vögeli and R. Riek, *J. Chem. Theory Comput.*, 2012, **8**, 3483-3492.
14. B. Vögeli, *J. Magn. Reson.*, 2013, **226**, 52-63.
15. I. Solomon, *Phys. Rev.*, 1955, **99**, 559-565.
16. G. J. Boender, S. Vega and H. J. M. de Groot, *J. Chem. Phys.*, 2000, **112**, 1096-1106.
17. K. H. Mroue, Y. Nishiyama, M. K. Pandey, B. Gong, E. McNerny, D. H. Kohn, M. D. Morris and A. Ramamoorthy, *Sci. Rep.*, 2015, **5**, 1-10.
18. T. Manolikas, T. Herrmann and B. H. Meier, *J. Am. Chem. Soc.*, 2008, **130**, 3959-3966.
19. D. Strotz, J. Orts, C. N. Chi, R. Riek and B. Vögeli, *J. Chem. Theory Comput.*, 2017, **13**, 4336-4346.
20. P. Rovó, C. A. Smith, D. Gauto, B. L. de Groot, P. Schanda and R. Linser, *J. Am. Chem. Soc.*, 2019, **141**, 858–869.
21. T. Gullion, *Chem. Phys. Lett.*, 1995, **246**, 325-330.
22. E. T. Olejniczak, S. Vega and R. G. Griffin, *The J. Chem. Phys.*, 1984, **81**, 4804-4817.
23. E. Nimerovsky and A. Goldbourt, *J. Magn. Reson.*, 2012, **225**, 130-141.
24. R. Zhang, Y. Nishiyama, P. Sun and A. Ramamoorthy, *J. Magn. Reson.*, 2015, **252**, 55-66.
25. S. K. Vasa, H. Singh, P. Rovó and R. Linser, *J. Phys. Chem. Lett.*, 2018, **9**, 1307-1311.
26. P. Rovó and R. Linser, *ChemPhysChem*, 2018, **19**, 34-39.
27. S. K. Vasa, H. Singh, K. Grohe and R. Linser, *Angew. Chem., Int. Ed.*, 2019, **58**, 5758-5762.